BRDF Measurements and Analysis of Retroreflective Materials

Laurent Belcour,[1,2,*] Romain Pacanowski,[3,†] Marion Delahaie,[4] Aude Laville-Geay,[4] and Laure Eupherte[4]

[1] *Inria Bordeaux Sud-Ouest, 200 avenue de la Vieille Tour, 33405, Talence, FRANCE*

[2] *Universite de Montréal, 2920 chemin de la Tour, Montréal, QC, CANADA*

[3] *CNRS, Esplanade des Arts et Métiers, 33402 Talence, FRANCE*

[4] *CEA, 15 avenue des sablières, 33116 Le Barp, FRANCE*

compiled: November 17, 2014

We compare performance of various analytical retroreflecting BRDF models to assess how they reproduce accurately measured data of retroreflecting materials. We introduce a new parametrization, the back vector parametrization, to analyze retroreflecting data and we show that this parametrization better preserves the isotropy of data. Furthermore, we update existing BRDF models to improve the representation of retroreflective data.

OCIS codes: (290.1483) BSDF, BRDF, and BTDF. (120.5700) Reflection. 120.5820 Scattering measurements. (290.1350) Backscattering

http://dx.doi.org/10.1364/XX.99.099999

1. Introduction and Motivation

The BRDF $\rho(\theta_i, \phi_i, \theta_o, \phi_o)$ is a radiometric quantity introduced by Nicodemus et al. [1] , which is used in the infrared as well as the visible domain, to characterize material reflectance properties. Intuitively, the BRDF represents, how the light is angularly reflected by a material per wavelength.

Formally, if we consider a small element of surface dA illuminated by an incident radiant flux $d\Phi_i$ from the direction $\mathbf{l} = (\theta_i, \phi_i)$ within the differential solid angle $d\omega_i$, and observe the reflected radiance flux around $\mathbf{v} = (\theta_o, \phi_o)$ within the differential solid angle $d\omega_o$, the BRDF is then defined as:

$$f_r(\theta_i, \phi_i, \theta_o, \phi_o)\, \cos\theta_o\, d\omega_o = \frac{d\Phi_o(\theta_o, \phi_o)}{d\Phi_i(\theta_i, \phi_i)}. \qquad (1)$$

As shown in the previous equation the BRDF is expressed in inverse steradians $[sr^{-1}]$. Our mathematical notations are illustrated in Figure 1.

The definition in Equation (1), which differs (but mathematically equivalent) from the one introduced by Nicodemus et al., shows that BRDF measurements cannot be directly done. First, measuring infinitesimal quantities is not possible. Therefore, it is better to assume that BRDF measurements represent the integral of the BRDF over a *finite* solid angle ($\Delta\omega_0$). The solid angle $\Delta\omega_o$ is directly related to the size of the detector used for the measurements. Second, goniophotometers or gonioreflectometers measure flux ratios that are proportional to the BRDF multiplied by a cosine factor ($\cos\theta_o$) and not the BRDF itself.

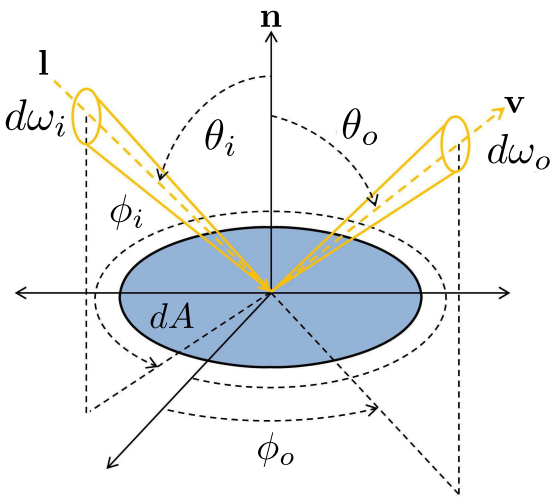

Fig. 1. The different vectors $(\mathbf{l}, \mathbf{v})$ and angles $(\theta_i, \phi_i, \theta_o, \phi_o)$ used in this paper to parametrize the different BRDF models. The vector $\mathbf{n}$ represents the surface normal and dA is the differential surface area on which the measurement with the detector is accomplished.

In this paper we focus on a particular and less-studied class of materials: retroreflective materials. Retroreflection is important and arises in different situation. They

* laurent.belcour@umontreal.ca

† romain.pacanowski@institutoptique.fr

are used for the safety of highway pavement [2, 3] and for safety clothes. Retroreflection also arises in nature: from biological tissues [4], tree canopy [5], rough surfaces [6] or dielectric layered materials [7].

Previous work have been dedicated to measure BRDF either with non-imaging systems (e.g., [8–15]) or with imaging systems (e.g., [16–24]), which are becoming more and more popular due to the low cost of digital cameras. However, few (e.g., [12–15]) of them are capable of measuring retroreflective materials due to mechanical constraints. This comes from the fact that the illumination direction and the sensor direction must be aligned (i.e., $\mathbf{l} = \mathbf{v}$). In this paper, we present our own retroreflection BRDF acquisition device along with our measurements (cf. Section 2) and we take advantage of these new measurements to extend the study of retroreflective materials. More precisely, we make the following contributions:

- A new parametrization useful to represent measured materials with retroreflecting lobes (cf. Section 3). We show that this parametrization preserves the isotropy or anisotropy of the data.
- Improvements of existing BRDF models so that they support retroreflection phenomenon (cf. Section 4).
- Multiple comparisons of the capabilities of existing and improved BRDF models to represent retroreflective material measurements using fitting and approximation techniques (cf. Section 5).

2. Retroreflection Measurements

2.A. Retroreflection BRDF Capture Setup

Our measurement device, developed at CEA-CESTA, is built upon a classical BRDF gonioreflectometer (e.g. [8–11]). A goniometric cradle, a rotation stage and a rotating arm are used to provide the three degrees of freedom required to measure an isotropic BRDF (cf. Figure 2). The goniometric cradle and the rotation stage control the direction of incidence of the light source. More specifically, the goniometric cradle permits to measure (light,detector) configurations, which are outside the plane of incidence. The rotating arm is mainly responsible for moving the detector. The light source is a 10mW HeNe laser (633 nm) and is collimated on the sample to be measured with two mirrors acting as a beam steerer. The detector used is a 400-900nm photodiode manufactured by Hammamasu (model C10439-01) which size is $2.4 \times 2.4\, mm^2$ (the solid angle subtended by the detector when placed at the beam splitter position is approximately 3.6e-5 sr^{-1}). To minimize the noise level, the incident beam generated by the laser is chopped at 230 Hz.

The main difference compared to a 3D isotropic gonioreflectometer is that the detector does not occlude the incoming light source (i.e., the laser). As shown in the right part of Figure 2, this is achieved by using a 70-30 beam splitter. This splitter and the detector are fixed on a metallic plate firmly connected to the rotating arm. The main principle is similar to the one used by Ruiz-Cortés and Dainty [15] or by Rabal et al. [14] or previously by Jordan [25]. This is a classical setup to achieve measurement in the retroreflective direction. The angular occluded zone (cf. holes in the graphics of the right part of Figure 3), which cannot be measured, is coming from the metallic plate holding the beam splitter and the detector.

All measurements have been made relatively to the measurement of a target Spectralon coming from LabSphere. The beam splitter has been characterized with FTIR spectrometer. This is necessary to rescale the measurements belonging to the retro-reflective zone by the transmission factor. Our measurement setup does not take into account polarization (i.e., the measure of the BRDF is the average measure over different polarization states).

2.B. Material Samples Measurements

We measured three retroreflective materials two coming from 3M and one from Avery Dennison: a yellow tape covered with plastic, a gray tape, and an orange tape (cf. Figure 3). These materials are often stitched on safety jacket to improve the visibility of workers during the night. According to the microscopic analysis returned by an optical interferometer (ZYGO Newview 7300), the structure of the Yellow tape material has two layers : one corresponds to the fabric whereas the other one contains micro-balls made of glass that are responsible for the retroreflective behavior. This implies that the optical interferometer is not able to recover the height field surface profile of the Yellow tape due to these two layers, this is not the case for the Orange coating and the Gray tape materials though.

Our setup permits to measure isotropic retroreflective BRDFs. Mathematically speaking, an isotropic BRDF requires only three angles to be parametrized: $f_r(\theta_i, \theta_o, \Delta\phi)$ where $\Delta\phi = \phi_i - \phi_o$. The isotropic BRDF multiplied by its cosine factor is measured on a set of discrete $(\mathbf{l}, \mathbf{v})$ configurations which are spanning configurations both inside and outside of the plane of incidence: $\rho_s(\theta_i, \theta_o, \Delta\phi) \cos\theta_o \Delta\omega_o$ where ρ_s represents the s-th measurement sample. For all materials, we used three angles of incidence for the light source direction (i.e., $\theta_i = \{15°, 30°, 60°\}$) Regarding the detector, we set $\theta_o \in [0°, 90°]$ with three degrees resolution step and $\Delta\phi \in [-180°, 180°]$ with a 10 degrees resolution step for the Yellow and Gray tapes. Since the Orange coating is a more complex material we measured it more densely: $\theta_o \in [0°, 90°]$ with two degrees resolution step and $\Delta\phi \in [-180°, 180°]$ with a 5 degrees resolution step. Furthermore, the mirror and retro-reflective directions have been measured even more densely to minimise sampling artefacts at the center of both lobes. For the Yellow and Gray tapes the total number of measured $\mathbf{l}, \mathbf{v}$ configurations is 3×3483 and 3×14554 for the Orange

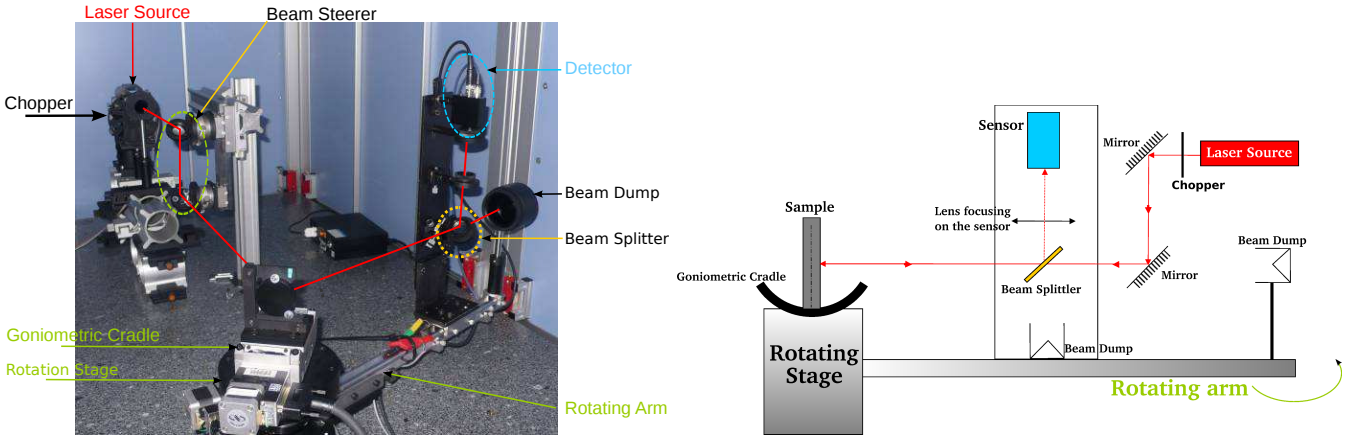

Fig. 2. Lateral view of our system to acquire retro-reflective materials. The principle is to use a beam splitter to avoid occlusion of the incident light source by the sensor when they are collinear. The incident beam is emitted from a laser source that goes through a beam splitter, which acts as a transparent glass, before being reflected by the sample. If the material reflects light backward (retro-reflection configuration), the scattered beam travels back to the beam splitter which is going to reflect it toward the sensor.

coating.

As shown in the right part of the Figure 3, the different measured materials present a specular lobe in the retroreflective (i.e., when the light source and detector are aligned) direction. The magnitude of the retroreflective lobe is higher than the one in the mirror direction. The Yellow tape material has even two lobes, one forward and one backward of approximately the same magnitude. As a general observation, the Gray tape and the Orange coating do have a more complex behavior with a strong BRDF magnitude decrease with respect to the angle of incidence.

3. Retroreflection Parametrizations

The parametrization plays an important role in the description, understanding and use of data. In this section, we describe the different parametrizations we used in our analysis of retroreflective materials. We recal the classical parametrization to describe retroreflection in Section 3.A. Then we introduce a new parametrization, the *back parametrization*, in Section 3.B. Finally, we compare those two parametrizations and show that the new parametrization permits to describe more efficiently the data (Sections 3.C and 3.D).

3.A. View Vector

Retroreflection can be specifically described by centering the parametrization around the view direction and looking at the angle between the view and light direction. To design distributions that are by construction reciprocal, it is useful to take as input the dot product between the light and view vectors clamped to positive values:

$$\cos_R = (\mathbf{l} \cdot \mathbf{v})^+, \tag{2}$$

where $\cdot$ denotes the dot product between two vectors and $(.)^+$ clamps a real value to the positive domain.

3.B. Back Vector

We introduce a new parametrization of the retroreflection domain, using a new direction vector: the *back vector*. We note it $\mathbf{b}$ and its formulation is:

$$\mathbf{b} = \frac{\mathbf{v}' + \mathbf{l}}{||\mathbf{v}' + \mathbf{l}||}, \tag{3}$$

where $\mathbf{v}' = 2(\mathbf{n} \cdot \mathbf{v})\mathbf{n} - \mathbf{v}$ is the symmetric of the view vector with respect to the normal vector, $\mathbf{n}$. Intuitively, the back vector is the halfway direction between the reflected direction $\mathbf{v}'$ and the light direction $\mathbf{l}$ (Figure 4). When used in a BRDF model, we use the dot product between the back vector and the normal to ensure reciprocity:

$$\cos_B = \mathbf{b} \cdot \mathbf{n}. \tag{4}$$

The use of the back vector is justified by considering microfacet theory [27]. We show in Appendix A, with a 1D example of a V-cavity microfacet surface, that the BRDF can be parametrized using the back vector.

3.C. Comparison of parametrizations

The two parametrizations can be compared using a pseudo-planar formulation:

$$(\mathbf{l}, \mathbf{v}) \rightarrow (\theta_i, \theta\cos(\Delta\phi), \theta\sin(\Delta\phi)),$$

where θ is either the angle between the view and light vectors or the back and normal vector, and ϕ is the azimuth between the light and view vectors or of the back vector.

We compare the impact of the parametrization on the data in Figure 5 by displaying the isoline of the data in the parametrization's planar formulation. It provides an intuitive way to view how a parametrization deforms the data. In the next section we provide a quantitative study of this deformation using moments analysis.

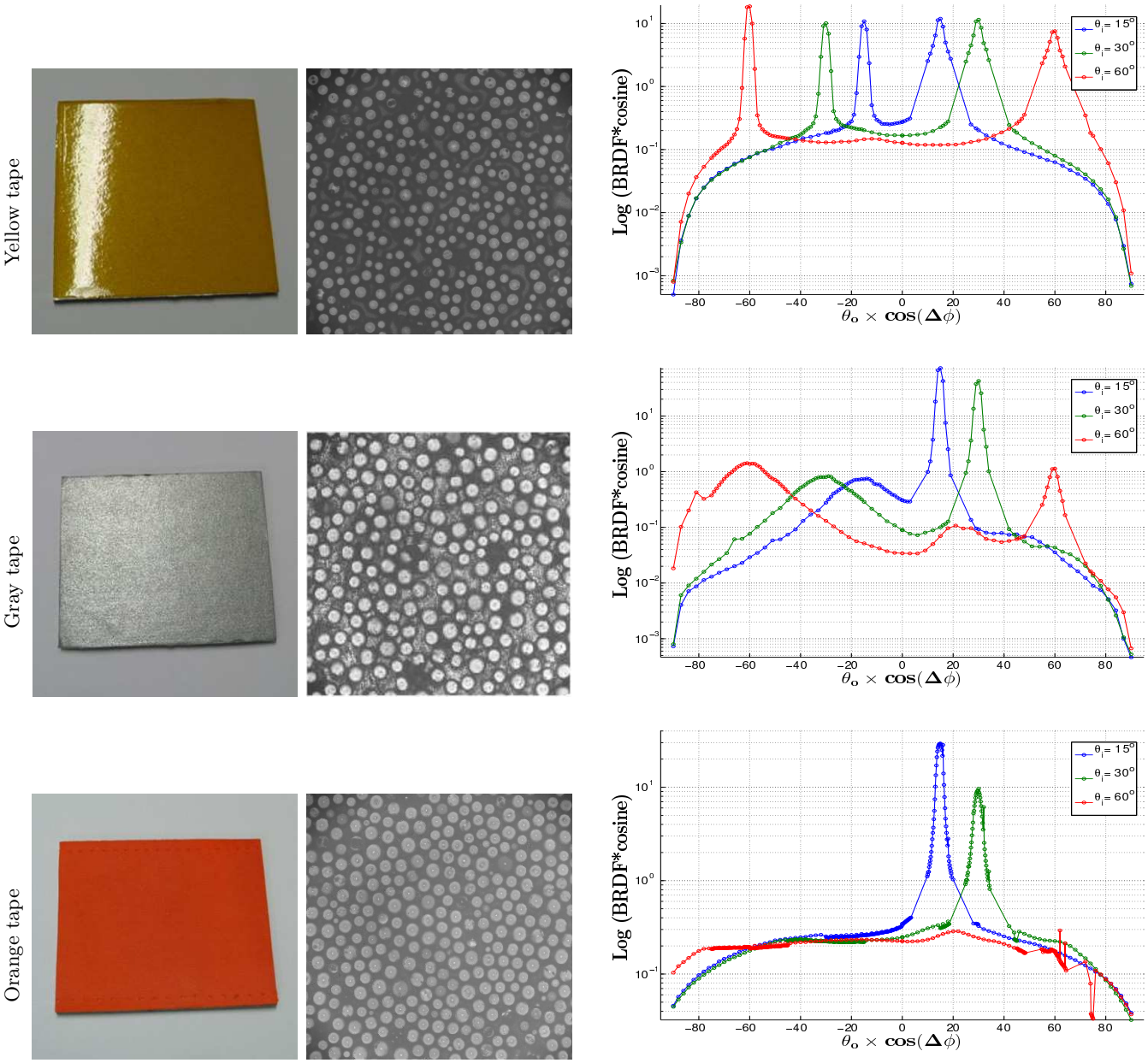

Fig. 3. The three retro-reflected materials. **Left**: photographs of the samples. **Center**: Optical Surface Profiler (NewView 7300) images revealing the micro-balls structure of the retro-reflective materials. However, since the Yellow tape has an additional layer in top of the micro-balls structure, the interferometer cannot exactly extracts the height-field corresponding to the micro-balls layer. **Right**: BRDF corrected by the cosine factor measurements in the plane of incidence ($\Delta\phi = 0°$ or $\Delta\phi = 180°$) where the retroreflective zone corresponds to positive abscissa values (i.e., $\theta_0 \cos\Delta\phi \geq 0$). For the Orange tape at 60-degree incidence, the outliers present around $\theta_o \cos(\Delta\phi) = 60°$ and $\theta_o \cos(\Delta\phi) = 75°$ have been removed for the rest of the study.

3.D. Moments analysis

A parametrization that preserves the data isotropy or anisotropy allows to compress the data a little more and is more stable with respect to fitting.

To study the anisotropy of our data, we analyze the retroreflective specular lobe and compute its central moments in the two parametrizations with respect to the input elevation. The formulation of central moments in those 2D parametrizations is:

$$\mu_{i,j}(\theta_i) = \frac{1}{||f||} \int (x - \mu_x)^i (y - \mu_y)^j f(\theta_i, x, y) dx dy, \quad (5)$$

where $(x, y) = \big(\theta\cos(\Delta\phi), \theta\sin(\Delta\phi)\big)$ denote the coordinates of the 2D parametrization, and (μ_x, μ_y) is the

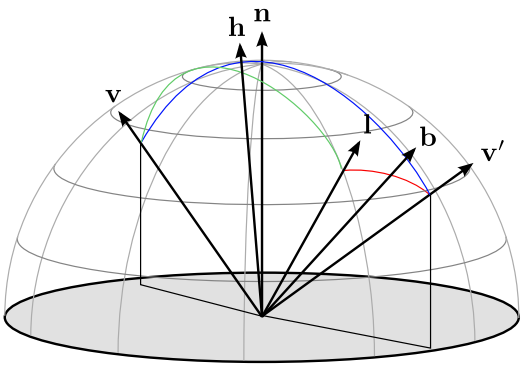

Fig. 4. We introduce the back vector, **b**, which is half-way between the light vector and the vector $\mathbf{v}'$, which is the symmetric vector of **v** with respect to the normal **n**. It shares properties with **h**, the half-vector (cf. [26]) that is used in the microfacets theory introduced by Torrance and Sparrow [27].

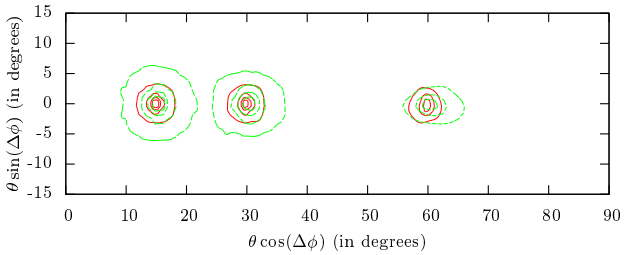

Fig. 5. We analyze the isolines of the interpolated yellow cloth data in the back (red) and light-view (green, dashed) parametrizations with respect to the angle of incidence. Isolines have been shifted by the angle of incidence for clarity. The back parametrization keeps the data more uniform with respect to the angle of incidence compared to the light-view parametrization.

mean vector. The $\frac{1}{||f||}$ weight ensures proper normalization. The diagonal terms of the second central moment, $\sigma_x^2 = \mu_{2,0}$ and $\sigma_y^2 = \mu_{0,2}$ correspond to axis variances. The fourth central moment diagonal terms, $\mu_{4,0}$ and $\mu_{0,4}$, are link to the axis kurtosis. They indicate if the distribution is more 'peaked' or 'flattened' than the Normal distribution. Non diagonal terms (i.e. i and j different from zero) relates to the correlations of the function between the dimensions of the parametrizations. Non diagonal terms close to zero indicate a close to separable behavior of the data.

In Figure 6, we compare how the two parametrizations preserve the isotropy of the data. To do so, we investigate how the ratio of the x and y variances evolves as the input incidence increases. To keep the plot coherent (in the $[0, 1]$ domain, 0 corresponding to perfect isotropy), we look at the ratio between the difference of the x and y variances and the maximum variance. The newly introduced back parametrization preserves the isotropy of the retroreflective lobe better. We noted the exception of the grazing incidence of the Orange coating sample. However, at this incidence, the Orange cloth sample is not unimodal (see Figure 10(a)) perturbing the moment analysis.

Both parametrization provide low covariance values (i.e., two orders of magnitude below the variances). Thus, both parametrizations will provide a good separability of the data along their axis. This property is important for fitting using basis functions (such as rational polynomials) as it allows a greater compression of the data.

All samples showed a strong kurtosis, being spikier or flatter than a Gaussian function. This predicts that Gaussian profiles will not provide good fits and this prediction is confirmed by our fitting results.

4. BRDF models for retroreflection

4.A. Existing BRDF models for retroreflection

Different BRDF models account for retroreflection in the literature. Some provide a direct comprehension of the retroreflection by resolving the light transport on simplified geometry. Other BRDF models, often empirical ones, handle retroreflection by construction.

a. Numerical models. Trowbridge [28] derived the retroreflection of light from right angle corners, inclusions, and below surface shadowing. Proposed models are incompatible with our data as they exhibit a singularity in the pure retro direction and thus are not suited for fitting. Moreover, those models are expensive to compute and do not contain any shadowing or Fresnel term. Stoudt and Vedam [2, 3] as well as Grosges [29] elaborated numerical retroreflective models in the case of glass beads inclusion in road paints. Those models are not suited for data fitting due to their numerical nature. More recently, first and second order Kirchhoff approximations were proposed to describe the back-scattering from rough surfaces [6, 30]. Unfortunately, those derivations do not provide a closed formula [31] and only provide insight for a small portion of backscattering surfaces.

b. Analytical models. Yoo et al [4] provided a Gaussian formulation of retroreflection from a monochromatic light on biological tissues depending on the albedo and mean free path of the medium. Simple formulations exist to simulate diffused pitted surfaces [32]. Retroreflection from randomly oriented microfacets [33] has been used to explain the appearance of the moon but does not apply in the case of retroreflective garments. Modeling the hotspot effect on forest canopy is usually done by considering the geometry of leaves, branches and tress. Unfortunately, a closed form model of forest BRDF is usually not available [34]. For efficiency reasons, empirical Gaussian models are used [5].

c. Empirical models. Some empirical models include retroreflection as part of their degrees of freedom.

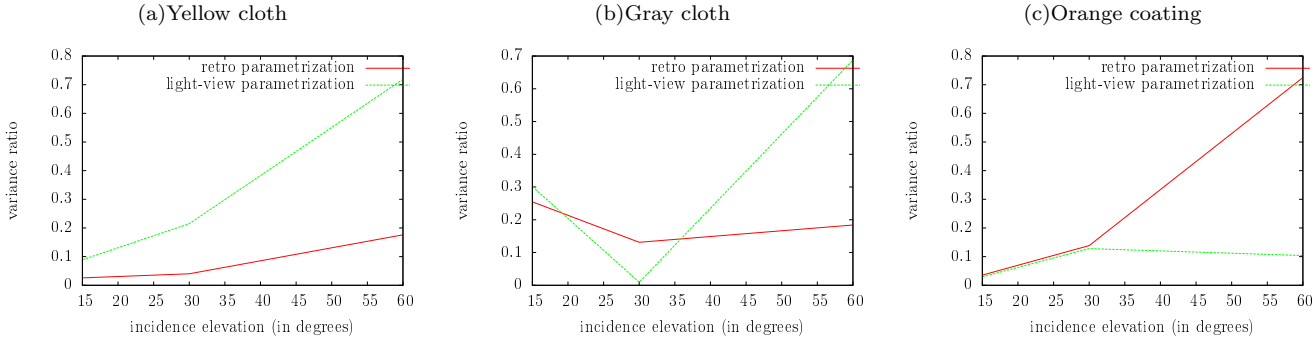

Fig. 6. We compare the ratio of variances $r = \frac{\sigma^2_{max} - \sigma^2_{min}}{\sigma^2_{min}}$ along the two axes of the planar parametrization for each sample for the three θ_i incidences of measure. Values close to zero denote perfect isotropy of the data while values close to one denote a strong anisotropy of the data. The back parametrization (red plain line) is more stable than the light-view parametrization (green striped line) for the Yellow and Gray samples, but fails to preserve isotropy for grazing incidences on the Orange sample. For this last sample, the data is clearly not composed of a single lobe and there is not a simple retroreflection model that could explain it (cf. Figure 10(a)). We performed the moment analysis only on the data of the retroreflective lobe (when possible) to preserve a unimodal shape.

The generalized cosine mode from Lafortune et al. [35] can model retroreflection using its transformation matrix (using $C_x = C_y > 0$). Neumann and Neumann's BRDF [36] provide retroreflection using the same transformation mechanism, but lacks a close formulation.

d. Basis models. Other models provide a surface representation of the BRDF by mean of a functional basis, they are used to project the data onto them. Pacanowski et al. [37] use rational functions in the half vector parametrization. Spherical harmonics are often used as a way to describe angular distribution [38] but are restricted to low frequencies. Wavelets [39] provide the compression capabilities to store high frequency materials but the lack of efficient and practical basis functions limit their capabilities to describe a signal on the sphere. Generally, as shown by Mahajan et al. [40], the number of coefficients for Spherical Harmonics or Wavelets grows quadratically with the frequency of the signal that needs to be represented.

e. Summary. We could not identify any retroreflecting BRDF model from the literature that could match our requirements. Analytical models are restricted to diffuse surfaces or simple lobes (either cosine or Gaussian) and do not model Fresnel or Shadowing effects. Models that would produce such behaviors require costly numerical evaluations and are not suitable for use in computer programs (like parameters finding) that require a lot of evaluations of the BRDF.

We decided to compare the performance of four different parametric BRDF models and a semi-parametric model: an extended cosine model [35], a Blinn lobe [26], a Beckmann distribution [41], an ABC distribution [42], and a Rational function [37]. Since some of these BRDFs cannot model the retroreflection, we decided to improve them (Section 4.B) by expressing them in one adapted to the retroreflection parametrization (Section 3). Furthermore, since some models could not express the Fresnel or the Shadowing effect, we decided to add a retroreflective Fresnel term (Section 4.C) and a Smith [43] shadowing term when needed.

4.B. Updating existing BRDF Models

Using the formulation of the Back vector, we provide new empirical models to approximate retroreflective data efficiently. In all the following, BRDFs f_r are decomposed into a single scattering term, f, a retroreflective term, f_b, and an incoherent (diffuse) scattering term, f_d: $f_r = f + f_b + f_d$. We also denote c either the *view* vector or the *back* vector parametrization cosine $\cos_{RB} = \{\cos_R, \cos_B\}$.

4.B.1. Simple Cosine

The simple cosine model (also referred as Blinn BRDF [26]) uses the power of the dot product between the Half vector and the normal of the surface to model the BRDF:

$$f = (\mathbf{h} \cdot \mathbf{n})^{\alpha}. \tag{6}$$

We extend this model and provide a retroreflective BRDF by replacing the Half vector with one of the retroreflection cosines:

$$f_b = \cos^{\alpha}_{RB}\,. \tag{7}$$

This model has the benefit to be computationally efficient as dot products are fast to compute. Efficient BRDF models permit to use non local parameter research algorithms such as controlled random search [44].

4.B.2. Beckmann Distribution

Microfacet theory [27] describes the reflection of light on a surface modeled as distribution of oriented mirrors. Assuming that the distribution of the microfacet

normals follows the Normal distribution (referred as the Beckmann distribution [41]), single scattering formulation is (presented in the Half angle parametrization):

$$f = \frac{D(\mathbf{h})F(\mathbf{v}\cdot\mathbf{h})G(\mathbf{l},\mathbf{v},\mathbf{h})}{4(\mathbf{l}\cdot\mathbf{n})(\mathbf{v}\cdot\mathbf{n})},$$

where F denotes the Fresnel term, G accounts for the visibility of micro-geometry from the input and output directions, and $D(\mathbf{h})$ is the distribution of microfacets (as defined in Walter et al. [45]):

$$D(\mathbf{h}) = \frac{1}{\pi\alpha^2(\mathbf{h}\cdot\mathbf{n})^4}\exp\left(\frac{(\mathbf{h}\cdot\mathbf{n})^2-1}{\alpha^2(\mathbf{h}\cdot\mathbf{n})^2}\right),$$

where α is the surface roughness.

We introduce a f_b term which include retroreflection into the microfacet reflection model using the same mathematical form than f:

$$f_b = \frac{D_b(\mathbf{b})F_b(\mathbf{v},\mathbf{b})G(\mathbf{l},\mathbf{v},\mathbf{h})}{4(\mathbf{l}\cdot\mathbf{n})(\mathbf{v}\cdot\mathbf{n})},$$

The retroreflective distribution term, D_b, is modeled by replacing the dot product between the Half vector and the normal by one of the retroreflection cosine:

$$D_b(\mathbf{b}) = \frac{1}{\pi\alpha^2\cos_{RB}^4}\exp\left(\frac{\cos_{RB}^2-1}{\alpha^2\cos_{RB}^2}\right).$$

Note that the α used in the retroreflective formulation is no longer the micro-surface roughness. It however defines the apparent roughness of the retroreflection. We describe our retroreflecting Fresnel term F_b and discuss the shadowing/masking term G in Section 4.C.

4.B.3. ABC Model

Church et al. [42] introduced the ABC parameters to recover a BRDF from surface profile measurements based on the Rayleigh-Rice theory. For efficient fitting and evaluation of data Löw et al. [46] derived a new microfacet BRDF model, which distribution relies on the ABC parameters. We use their formulation:

$$f = \frac{A}{\big(1+B(1-(\mathbf{h}\cdot\mathbf{n}))\big)^C}F(\mathbf{v}\cdot\mathbf{h}).$$

We update the ABC model by changing the dot product between the Half vector and the normal by one of the retroreflection cosines and by changing the Fresnel term by a retroreflecting Fresnel term:

$$f_b = \frac{A}{\big(1+B(1-\cos_{RB})\big)^C}F_b(\mathbf{v}',\mathbf{b}).$$

4.C. Fresnel and Shadowing terms for retroreflection

During measurements, we experienced reflectance profiles in the backward direction similar to the one of the Fresnel effect in the forward direction for the Yellow sample (Fig. 10(c)). Following efficient formulations introduced in graphics [47], we provide a formulation for the Fresnel effect in the retroreflective lobe:

$$F_b(\mathbf{v}',\mathbf{b}) = F(\mathbf{v}'\cdot\mathbf{b}).$$

Instead of using $u = \mathbf{l}\cdot\mathbf{h}$, we use the product between $\mathbf{v}'$ and $\mathbf{b}$ ($u = \mathbf{v}'\cdot\mathbf{b}$), and use Schlick's approximation of the Fresnel $F(u), u\in[0,1]$. By definition this Fresnel term incorporates reciprocity which makes it straightforward to use.

We also experienced a strong shadowing effect during the measurement of the gray and orange samples. We experimented with Smith [43], Cook and Torrance [48], and Schlick's [47] approximation for shadowing functions, but none of them provided satisfactory results. We used Smith shadowing term for Gaussian profiles [43] in the two cases.

5. Comparison of BRDF models

In this section, we compare the performance of the various retroreflective BRDF models presented in Section 4. We first compare all parametric models (cf. Section 5.A) on the three data samples and then add a non-parametric model (cf. Section 5.B).

We perform the fitting procedure on the retroreflective domain of the BRDF ($\theta_o > 0$ in our case). This provides more stable optimizations procedure and reduce the number of data points to consider, reducing the cost of the optimization.

To estimate the parameters of a given parametric BRDF model, we perform a nonlinear optimization of the L^2 difference with respect to the parameters as the cost function:

$$\arg\min_{\mathbf{p}} \sqrt{\sum (f_{\mathbf{p}}(\mathbf{x}_s)-\rho_s)^2}. \tag{8}$$

In this equation, $f_{\mathbf{p}}$ is a BRDF model with parameters vector $\mathbf{p}$ and we optimize the square distance to the data values ρ_s acquired at positions $\mathbf{x}_s$. Most nonlinear solver optimize this L^2 norm as a first order formulation of the cost function is easy to compute, and enables local searches algorithms to be used.

Rational functions interpolate vertical segments and thus optimize a cost function close to the infinity norm. This implicit cost function is mixed with an explicit one on the coefficients: the algorithm tries to reduce the L^2 norm of the coefficient vector.

5.A. Parametric models

a. Yellow sample. The results of our fitting of parametric models on the yellow sample are reported in Figure 7. The yellow sample exhibits a kurtotic behavior that the ABC model correctly reproduces. This sample exhibits a strong Fresnel effect with an increase in intensity at grazing angles; we have therefore added our updated Fresnel term to perform the fitting.

We did not include the Fresnel term in the Lafortune model since it can already reproduce Fresnel behavior.

b. Gray and Orange samples. The results of our fitting of parametric models on the gray and orange samples are reported in Figure 8 and Figure 9. These samples exhibit a kurtotic behavior that the ABC model and the power of cosine correctly reproduce. Furthermore. Since these samples do not show sign of a Fresnel effect (increase of intensity at grazing angles), we did not add our updated Fresnel term to the fitting. However, these samples show a strong shadowing effect. We used Smith shadowing term for Gaussian profiles [43] in the two cases. We did not include a shadowing term in the Lafortune model since its formulation can already reproduce such behavior.

5.B. Rational Function Fitting

Rational functions have no issue dealing with retroreflective data when given a reasonable number of coefficients. We performed the interpolation (cf. Figure 10) of the Yellow tape sample with 48 coefficients for a three dimensional data set. This is coherent with what Pacanowski et al. [37] reported. Since we perform the fitting on the three dimensional data, we can retrieve the complete BRDF. For our rational approximations, we used an absolute error of 0.5 with respect to the data and kept the solution minimizing the L^2 norm for the Yellow and Gray samples. For the Orange coating, we used a larger absolute error of 1.0 to obtain reasonable approximations (with less than a hundred coefficients). We compared the benefit of performing the approximation in the back or light-view parametrization. Our experiment show no real gain to use the back parametrization. Note that since the rational fitting does not optimize for the L^2 norm, there might exists better solutions for one or the other parametrization. Finally, we did not use the apparent separability, validated by the moment analysis, of our data in the projected plane to further reduce the number of coefficients. Since the data is close to separable in both parametrizations, fitting could be perform independently along the two dimension of the projective plane. This would reduce the number of coefficients as all cross terms would not appear in the formulation of the BRDF.

5.C. Summary

We report the different L^2 norms (see Equation 8) in Table 1. These norms are computed with respect to densified data sets. We interpolate missing values and made the samples more regular in the projected space. Although this create a bias in regions where the data could not be measured, it also makes the L^2 norm close to the continuous L^2 norm in regions where the signal was sufficiently measured.

Comparing the models, Rational functions perform the best both on the L^2 norm and the L^∞ norm (not reported). However, Rational functions parameters cannot be connected to a physical explanation of the measurements. The ABC model provides a good fitting of the yellow sample. For the gray and orange data, the Lafortune BRDF provides better fits. This is because we were not able to design an adequate shadowing term for the retroreflection and that the Lafortune BRDF can model this decrease in intensity with respect to the incidence elevation.

Overall, despite its good mathematical property of being more uniform, the advantage of the back parametrization in terms of fitting is not clear. The L^2 error values are relatively close between the two parametrizations and we cannot discriminate one parametrization or the other with respect to fitting.

	Yellow tape	**Gray tape**	**Orange coating**
Lafortune	0.689	0.906	0.589
Blinn	**1.109** (1.109)	**1.165** (1.165)	**1.007** (1.007)
Beckmann	**1.505** (1.110)	**2.858** (2.218)	**1.442** (1.119)
ABC	**0.443** (0.454)	**1.163** (1.177)	**0.751** (0.780)
Rational	**0.092** (0.080)	**0.191** (0.189)	**0.256** (0.293)
	Nb coeffs = 48	Nb coeffs = 35	Nb coeffs = 70

Table 1. L^2 norm distance of the fitted BRDF models to the retroreflective data. We report in each cell the distance when using the Back parametrization model in bold when it exists and the classical parametrization inside parenthesis. The L^2 norm for the back parametrization models is displayed first and we display the L^2 norm for the light-view parametrization in parenthesis. For the rational functions, we display the number of coefficients used to achieve the interpolation using a maximum error of 0.5 (1.0 for the Orange coating).

6. Fitting methodology

In this section, we provide the practical details used for the moment analysis, the fitting, and the interpolation of the data.

6.A. Prior-treatment of data

a. Moment analysis. To perform the integration of the data as specified in Equation 5, we interpolate the missing values from neighboring samples using the interpolation package of Matlab (*griddata* function was used to perform cubic interpolation). We show the reconstructed surfaces and the captured data in Figure 11. To better compute the moment of the lobe and avoid pollution by the diffuse term, we removed from the computation the different ρ_s that are below a given threshold. Thus we only consider the specular response in the analysis.

b. Fitting and rational approximation. To ensure a better convergence of the fitting and interpolation procedures we densified the data and filled the missing part using Matlab interpolation toolbox. This reduces the probability of producing a rational function with a zero in the denominator inside the domain. For the parametric fitting, this makes the cost function closer to the true

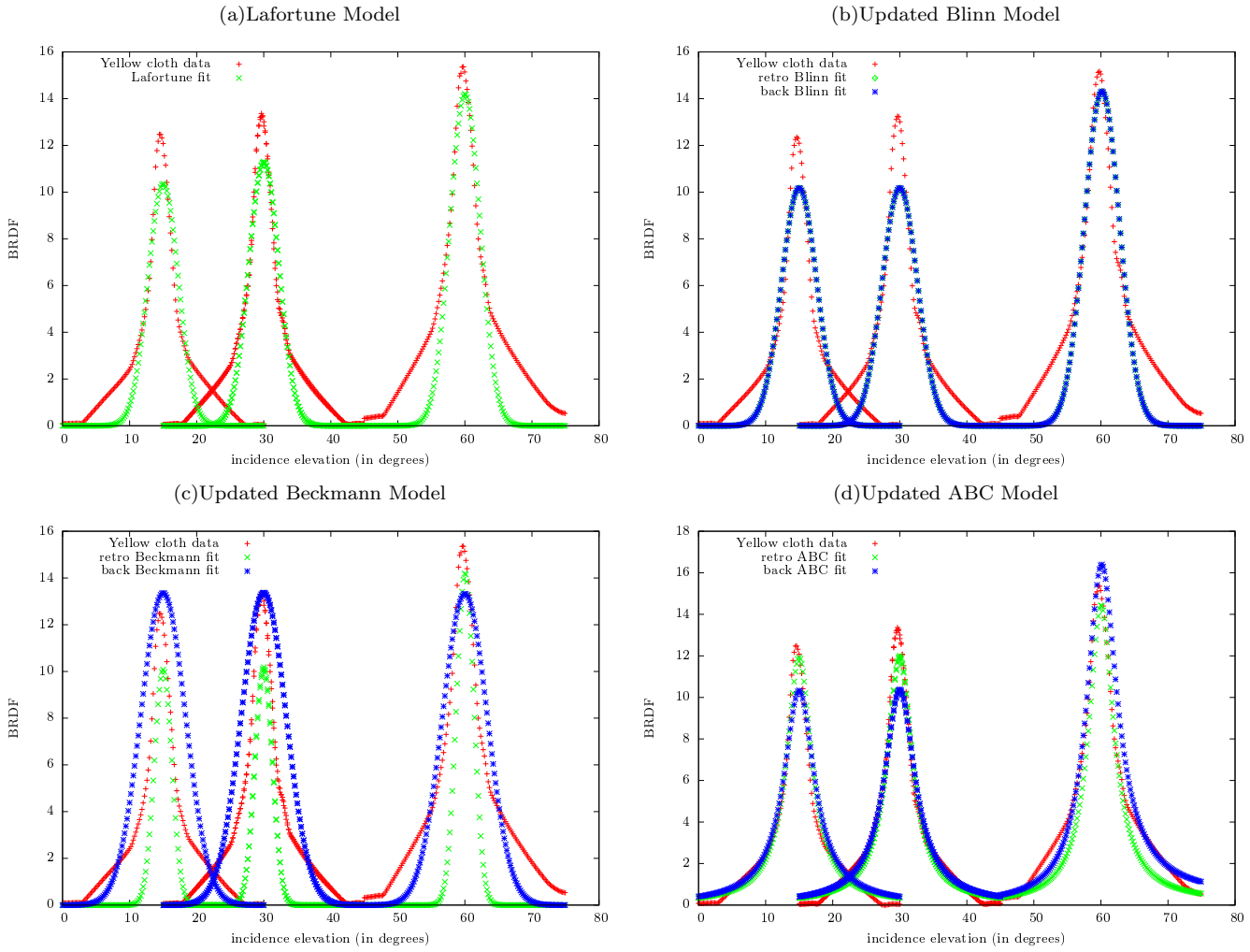

Fig. 7. Fitting comparisons of different updated BRDF models on the Yellow cloth sample. For clarity, we only display the domain where back scattering happens, $\theta_o > 0$, in the plane of incidence (*i.e.*, $\Delta\phi_o = 0$). All the incidences are outputted on the same plot. The updated ABC model is clearly the best fitting model for this data sample.

L^2-norm of the difference.

6.B. Algorithms

a. Parametric fitting. To perform our parametric fitting, we use the non-linear optimization library CERES [49]. This library performs optimization for nonlinear least-square problems.

b. Rational approximation. We use the rational interpolation of vertical segment from Pacanowski et al [37]. This approximation method relies on quadratic programming to find one of the possible solutions for a given set of vertical segments. We set our vertical segment to be at 0.5 around the data points and did not use the relative vertical segment advocated in this paper as it did not provide any stable fit in our case. We also clamp the vertical segment to be positive to avoid approximations with negative values, thus enforcing to fit a positive function. Furthermore, we use a cosine multiplied by a rational function to improve the stability of the approximation procedure.

7. Conclusion & Future work

a. Conclusion. By introducing the *back parametrization* for retroreflection, we improve existing BRDF models. The new parametrization preserves better the isotropy of data and allows to include a Fresnel term for the retroreflection. However, this new parametrization does improve only slightly the data fitting methods. We tested the performances of improved BRDF models for fitting and showed that a model close to ABC [42] was best describing the data. We showed that the masking term for retroreflection needs an analytical model.

b. Future work. A possible extension would be to improve our setup to acquire data more densely and by reducing even more the blind zone. This could help us to validate or discriminate our new parametrization and remove the influence of the reconstruction in the fitting

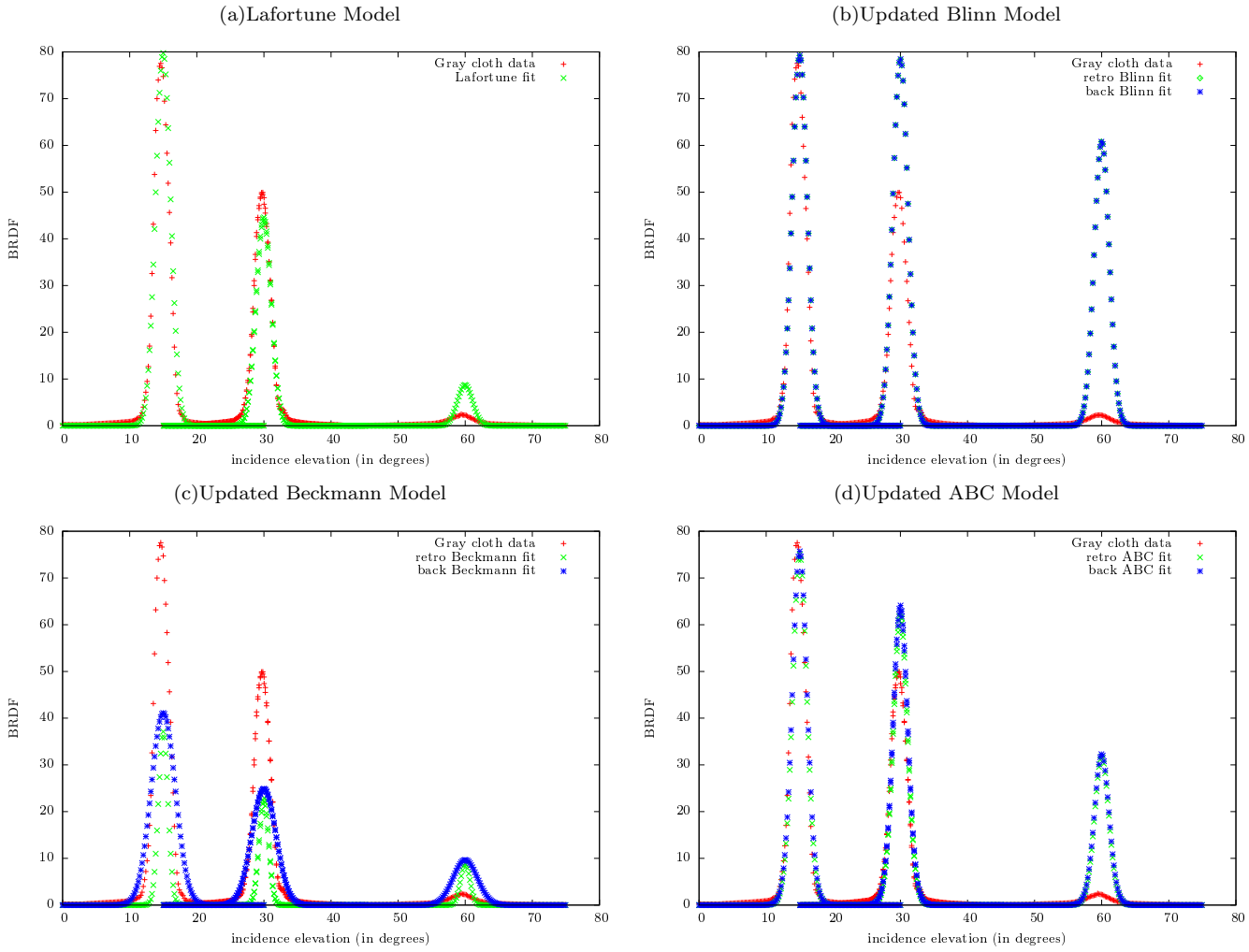

Fig. 8. Fitting comparisons of different updated BRDF models on the Gray cloth sample. For clarity, we only display the domain where back scattering happens, $\theta_o > 0$, in the plane of incidence (*i.e.*, $\Delta\phi_o = 0$). All the incidences are outputted on the same plot.

comparison. Another step in our research will be to provide an efficient and analytical retroreflection model with parameters connected to the physical phenomenon. From our study, we know that the shape of the retroreflection lobe can be explained by kurtotic models like the ABC model. The Fresnel term can be modeled using our extended model, but we currently lack a masking term. A new analytical model has to match those constraints. Finally, our fit and models could be of interest to other communities such as the computer graphics community, where no model for retroreflection is currently used.

Acknowledgments

The authors thank Christophe Schlick for his help during the early phase of this project and for introducing the term back vector. This work was supported by the ANR-11-BS02-006 grant *ALTA*.

Appendix A: A 1D Justification for the Back Vector

In this appendix, we provide a justification for the use of the back vector for retroreflecting data using results from the work of Torrance and Sparrow [27]. We only provide here a simplified 1D formulation of the scattering problem. Let us consider a surface and a double bounce of light given the incoming ($\mathbf{l}$) and outgoing ($\mathbf{v}$) directions as described in Figure 12. We assume that the surface is composed of a V-cavity of angular opening 2α aligned with the normal of the surface $\mathbf{n}$. We denote $\mathbf{m_v}$ the normal of the facet that $\mathbf{v}$ reflects on, and $\mathbf{m_l}$ the normal of the facet that $\mathbf{l}$ reflects on (Figure 12, in blue). Both cases describe the same angle with respect to the normal: $\mathbf{m_v} \cdot \mathbf{n} = \mathbf{m_l} \cdot \mathbf{n} = \cos(\alpha)$. Given $\mathbf{l}$ and $\mathbf{v}$, there is only one angle α for which the light will pass through. To determine α, we formulate the constraint that light coming from direction $\mathbf{l}$ must bounce on facet $\mathbf{m_l}$ in the opposite direction than the light bouncing on facet $\mathbf{m_l}$ from direction $\mathbf{v}$. The change of sign is equiv-

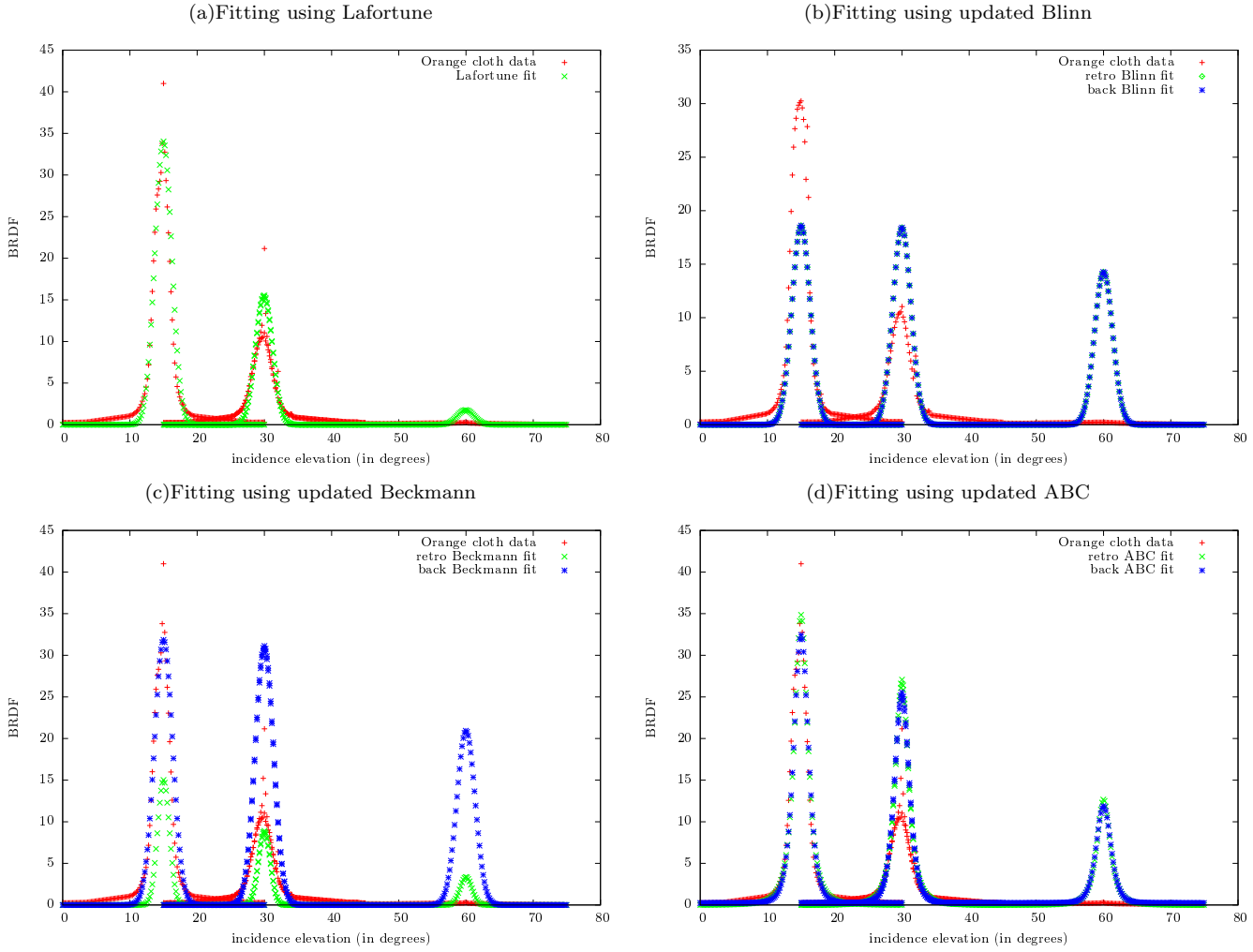

Fig. 9. Fitting comparisons of different updated BRDF models on the Orange cloth sample. For clarity, we only display the domain where back scattering happens, $\theta_o > 0$, in the plane of incidence (*i.e.*, $\Delta\phi_o = 0$). All the incidences are outputted on the same plot.

alent to a double symmetry of the resulting direction, a first symmetry with respect to the axis of the cavity (Figure 12, vertical dashed line) and a second symmetry with respect to the surface plane (Figure 12, horizontal dashed line). The symmetric of the reflection of $\mathbf{v}$ on facet $\mathbf{m_v}$ with respect to the cavity axis is the reflection of $\mathbf{v}'$ on facet $\mathbf{m_l}$. Consequently, the constraint is equivalent to: *the reflection of* $\mathbf{v}'$ *on facet* $\mathbf{m_l}$ *(noted* $\mathbf{d}'$*) is the symmetric of reflection of* $\mathbf{v}$ *on facet* $\mathbf{m_l}$ *(noted* $\mathbf{d}$*) with respect to the surface plane.*

$\mathbf{d}'$ relationship to $\mathbf{d}$ is thus: $\mathbf{d}' = \mathbf{d} - 2(\mathbf{d}\cdot\mathbf{n})\mathbf{n}$. We can expand this expression using $\mathbf{d} = 2(\mathbf{l}\cdot\mathbf{m_l})\mathbf{m_l} - \mathbf{l}$ and $\mathbf{d}' = 2(\mathbf{v}'\cdot\mathbf{m_l})\mathbf{m_l} - \mathbf{v}'$. By taking the dot product of the resulting expression with the normal $\mathbf{n}$, we get:

$$2(\mathbf{m_l}\cdot\mathbf{n})\big((\mathbf{l}+\mathbf{v}')\cdot\mathbf{m_l}\big) = (\mathbf{l}+\mathbf{v}')\cdot\mathbf{n} \qquad \text{(A1)}$$

Equation A1 makes apparent the back vector $\mathbf{b}$, and we can rewrite it: $2\cos(\alpha)(\mathbf{b}\cdot\mathbf{m_l}) = \mathbf{b}\cdot\mathbf{n}$. Since all vector are defined in the scattering plane, we can write in local coordinates $\mathbf{m_l} = [-\cos(\alpha), 0, \sin(\alpha)]$. The resulting equation can be written (if $\mathbf{b}_z > 0$): $\frac{\mathbf{b}_x}{\mathbf{b}_z} = \frac{\sin(2\alpha)-1}{\cos(2\alpha)+1}$.

References

[1] F. E. Nicodemus, J. C. Richmond, J. J. Hsia, I. W. Ginsberg, and T. Limperis, "Geometric Considerations and Nomenclature for Reflectance," National Bureau of Standards (1977).

[2] M. D. Stoudt and K. Vedam, "Retroreflection from spherical glass beads in highway pavement markings. 1: Specular reflection." Applied optics **17**, 1855–8 (1978).

[3] K. Vedam and M. D. Stoudt, "Retroreflection from spherical glass beads in highway pavement markings. 2: Diffuse reflection (a first approximation calculation)." Applied optics **17**, 1859–1869 (1978).

[4] K. M. Yoo, G. C. Tang, and R. R. Alfano, "Coherent backscattering of light from biological tissues." Applied optics **29**, 3237–3239 (1990).

[5] E. Bruneton and F. Neyret, "Real-time Realistic Rendering and Lighting of Forests," Computer Graphics Fo-

(a)Yellow cloth interpolation

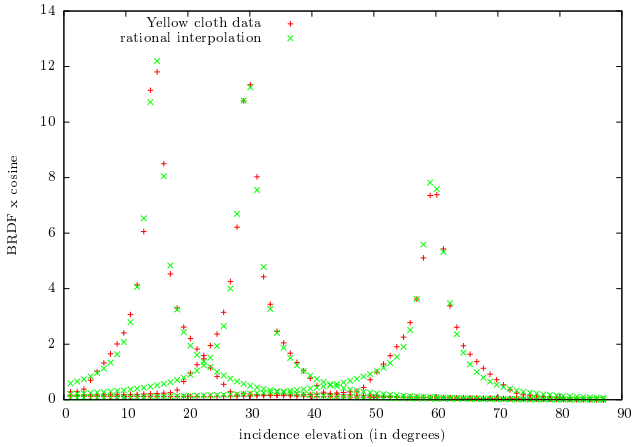

(b)Gray cloth interpolation

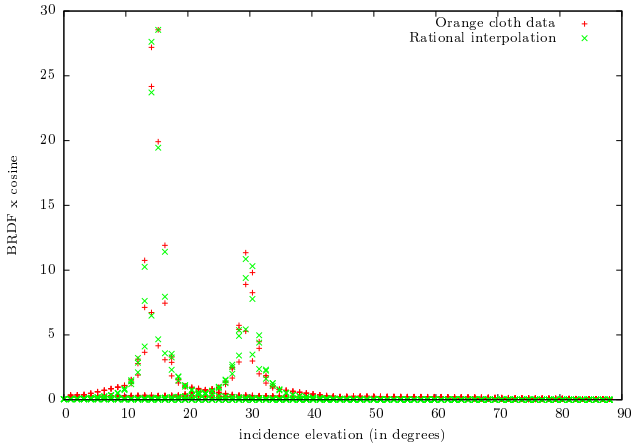

(c)Orange cloth interpolation

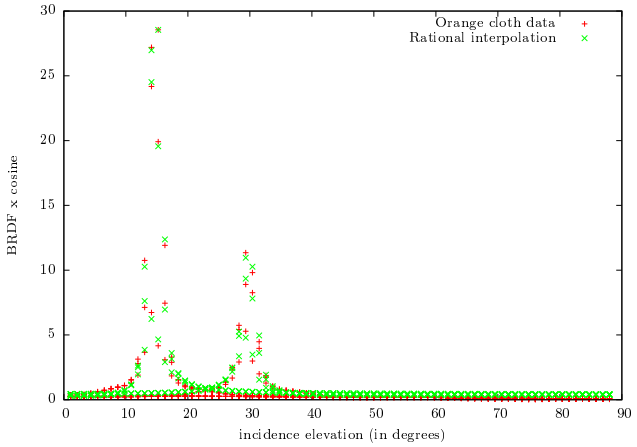

Fig. 10. Rational interpolation handles retroreflective data. We display the different fits we performed on the BRDF data, multiplied by the outgoing cosine, in the back parametrization. For clarity, we only display the domain where back scattering happens, $\theta_o > 0$, in the scattering plane (*i.e.*, $\Delta\phi_o = 0$).

rum **31**, 373–382 (2012).

[6] A. Ishimaru, C. Le, Y. Kuga, L. Sengers, and T. Chan, "Polarimetric scattering theory for high slope rough surface - Summary," Journal of Electromagnetic Waves and Applications **10**, 489–491 (1996).

[7] D. Blumberg, V. Freilikher, Y. S. Kaganovskii, A. Kotlyar, and A. A. Maradudin, "Backscattering of light from a dielectric layer on a reflecting substrate." Optics letters **29**, 1372–1374 (2004).

[8] D. R. White, P. Saunders, S. J. Bonsey, J. van de Ven, and H. Edgar, "Reflectometer for measuring the bidirectional reflectance of rough surfaces," Appl. Opt. **37**, 3450–3454 (1998).

[9] G. Serrot, M. Bodilis, X. Briottet, and H. Cosnefroy, "Presentation of a new brdf measurement device," Proceedings of SPIE **3494**, 34–40 (1998).

[10] G. Obein, R. Bousquet, and M. E. Nadal, "New NIST reference goniospectrometer," (2005), vol. 5880, pp. 58800T–10.

[11] D. Hünerhoff, U. Grusemann, and A. Höpe, "New robot-based gonioreflectometer for measuring spectral diffuse reflection," Metrologia **43**, S11–S16 (2006).

[12] T. J. Papetti, W. E. Walker, C. E. Keffer, and B. E. Johnson, "MRDF and BRDF measurements of low-scatter materials," in "Proceedings of SPIE," , vol. 6550 (2007), vol. 6550, p. 65500H.

[13] H. Iyota, H. Sakai, K. Emura, N. Igawa, H. Shimada, and N. Nishimura, "Method for measuring solar reflectance of retroreflective materials using emitting-receiving optical fiber," in "The Second International Conference on Countermeasures to Urban Heat Islands (SICCUHI)," , vol. 7 (2009), vol. 7, pp. 213–217.

[14] A. M. Rabal, A. Ferrero, J. Campos, J. L. Fontecha, A. Pons, A. M. Rubio, and A. Corrns, "Automatic goniospectrophotometer for the absolute measurement of the spectral brdf at in- and out-of-plane and retroreflection geometries," Metrologia **49**, 213–223 (2012).

[15] V. Ruiz-Cortés and C. Dainty, "Backscattering measurements from double-scale randomly rough surfaces," J. Opt. Soc. Am. A **29**, 1154–1160 (2012).

[16] G. J. Ward, "Measuring and modeling anisotropic reflection," in "Proceedings of the 19th Annual Conference on Computer Graphics and Interactive Techniques," (ACM, New York, NY, USA, 1992), SIGGRAPH '92, pp. 265–272.

[17] S. R. Marschner, S. H. Westin, E. P. F. Lafortune, and K. E. Torrance, "Image-based bidirectional reflectance distribution function measurement," Appl. Opt. **39**, 2592–2600 (2000).

[18] W. Matusik, H. Pfister, M. Brand, and L. McMillan, "Efficient isotropic brdf measurement," in "Proceedings of the 14th Eurographics Workshop on Rendering," (Eurographics Association, Aire-la-Ville, Switzerland, Switzerland, 2003), EGWR '03, pp. 241–247.

[19] S. Wadman and S. Baumer, "Appearance characterization by a scatterometer employing a hemispherical screen," Proceedings of SPIE **5189**, 163–173 (2003).

[20] A. Ngan, F. Durand, and W. Matusik, "Experimental analysis of brdf models," in "Proceedings of the Eurographics Symposium on Rendering," (Eurographics Association, 2005), pp. 117–226.

[21] C. Hahlweg and H. Rothe, "Design of a full-hemispherical spectro-radiometer with high dynamic range for characterization of surface properties using

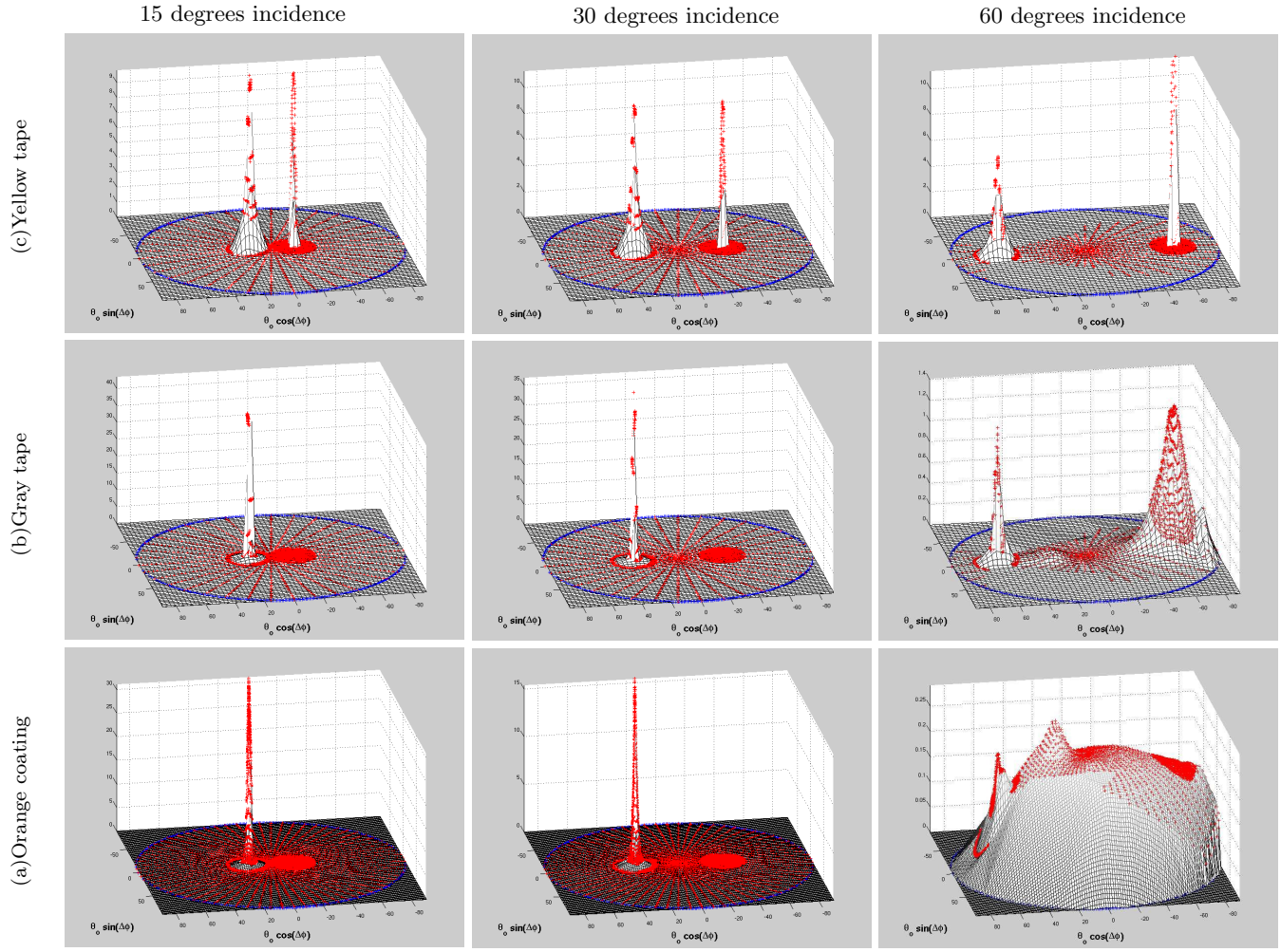

Fig. 11. 3D plot of the BRDF multiplied by the cosine factor for each measured material and for three different angles of incidence. Measurements are highlighted using red dots, while the reconstructed surfaces data we use for our analysis is displayed in gray-scale. The retroreflective zone corresponds to positive abscissa values (i.e., $\theta_0 \cos\Delta\phi \geq 0$).

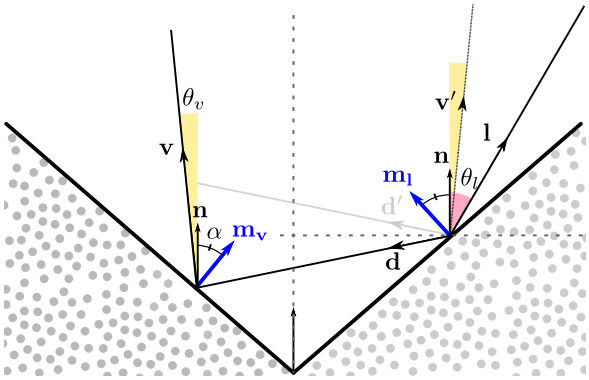

Fig. 12. We justify the use of the back vector by considering a microfacet surface. In that case retroreflection is caused by a double bounce in the surface cavities. Assuming no internal masking, the resulting distribution is centered around the back vector.

multispectral brdf data from vis to nir," Proceedings of SPIE **5965**, 596519–13 (2005).

[22] Y. Mukaigawa, K. Sumino, and Y. Yagi, "High-speed measurement of brdf using an ellipsoidal mirror and a projector," in "IEEE Conference on Computer Vision and Pattern Recognition. CVPR," (2007), pp. 1–8.

[23] J. Ren and J. Zhao, "Measurement of a bidirectional reflectance distribution and system achievement based on a hemi-parabolic mirror," Opt. Lett. **35**, 1458–1460 (2010).

[24] M. Andersen, E. Stokes, N. Gayeski, and C. Browne, "Using digital imaging to assess spectral solar-optical properties of complex fenestration materials: A new approach in video-goniophotometry," Solar Energy **84**, 549–562 (2010).

[25] D. L. Jordan, "Experimental measurements of optical backscattering from surfaces of roughness comparable to the wavelength and their application to radar sea scattering," Waves in Random Media **5**, 41–54 (1995).

[26] J. F. Blinn, "Models of light reflection for computer synthesized pictures," ACM SIGGRAPH Computer Graph-

ics **11**, 192–198 (1977).

[27] K. Torrance and E. Sparrow, "Theory of Off-Specular Reflection From Roughened Surfaces," Journal of the Optical Society of America **57**, 1105–1114 (1967).

[28] T. S. Trowbridge, "Retroreflection from rough surfaces," J. Opt. Soc. Am. **68**, 1225–1242 (1978).

[29] T. Grosges, "Retro-reflection of glass beads for traffic road stripe paints," Optical Materials **30**, 1549–1554 (2008).

[30] C. Bourlier and G. Berginc, "Multiple scattering in the high-frequency limit with second-order shadowing function from 2D anisotropic rough dielectric surfaces: I. Theoretical study," Waves in Random Media **14**, 229–252 (2004).

[31] C. Bourlier and G. Berginc, "Multiple scattering in the high-frequency limit with second-order shadowing function from 2D anisotropic rough dielectric surfaces: II. comparison with numerical results," Waves in Random Media **14**, 253–276 (2004).

[32] J. J. Koenderink, A. J. Van Doorn, K. J. Dana, and S. Nayar, "Bidirectional Reflection Distribution Function of Thoroughly Pitted Surfaces," Int. J. Comput. Vision **31**, 129–144 (1999).

[33] M. Oren and S. Nayar, "Generalization of Lambert's reflectance model," in "Proceedings of ACM SIGGRAPH," (1994), pp. 239–246.

[34] J. Chen and S. Leblanc, "A four-scale bidirectional reflectance model based on canopy architecture," IEEE Transactions on Geoscience and Remote Sensing **35**, 1316–1337 (1997).

[35] E. Lafortune, S.-C. Foo, K. Torrance, and D. Greenberg, "Non-linear approximation of reflectance functions," in "Proceedings of ACM SIGGRAPH," (1997), pp. 117–126.

[36] L. Neumann and A. Neumann, "A New Class of BRDF Models with Fast Importance Sampling," Tech. Rep. TR-186-2-96-24, Institute of Computer Graphics and Algorithms, Vienna University of Technology, Vienna, Austria (1996).

[37] R. Pacanowski, O. S. Celis, C. Schlick, X. Granier, P. Poulin, and A. Cuyt, "Rational BRDF," IEEE transactions on visualization and computer graphics **18**, 1824–1835 (2012).

[38] S. H. Westin, J. R. Arvo, and K. E. Torrance, "Predicting reflectance functions from complex surfaces," ACM Computer Graphics **26**, 255–264 (1992).

[39] L. Claustres, Y. Boucher, and M. Paulin, "Wavelet Projection for Modelling of Acquired Spectral BRDF ," Optical Engineering **43**, 2327–2339 (2004).

[40] D. Mahajan, Y.-T. Tseng, and R. Ramamoorthi, "An analysis of the in-out BRDF factorization for view-dependent relighting," in "Proceedings of Eurographics," (Eurographics Association, 2008), pp. 1137–1145.

[41] P. Beckmann and A. Spizzichino, *The scattering of electromagnetic waves from rough surfaces* (Artech House Publishers, 1987).

[42] E. L. Church, P. Z. Takacs, and T. A. Leonard, "The prediction of BRDFs from surface profile measurements," Proceedings of SPIE **1165**, 136–150 (1989).

[43] B. Smith, "Geometrical Shadowing of a Random Rough Surface," IEEE Transactions on Antennas and Propagation **15**, 668–671 (1967).

[44] W. Price, "Global optimization by controlled random search," Journal of Optimization Theory and Applications **40**, 333–348 (1983).

[45] B. Walter, S. Marschner, H. Li, and K. Torrance, "Microfacet Models for Refraction through Rough Surfaces," in "Proceedings of Eurographics Symposium on Rendering," (2007), pp. 195–206.

[46] J. Löw, J. Kronander, A. Ynnerman, and J. Unger, "BRDF models for accurate and efficient rendering of glossy surfaces," ACM Transactions on Graphics **31**, 1–14 (2012).

[47] C. Schlick, "An Inexpensive BRDF Model for Physically-based Rendering," Computer Graphics Forum **13**, 233–246 (1994).

[48] R. L. Cook and K. Torrance, "A Reflectance Model for Computer Graphics," ACM Transactions on Graphics **1**, 7–24 (1982).

[49] S. Agarwal, K. Mierle, and Others, "Ceres solver," `http://ceres-solver.org/` (2014).